

7

TRANSMISSION ELECTRON MICROSCOPY AND COMPUTER-AIDED IMAGE PROCESSING FOR 3D STRUCTURAL ANALYSIS OF MACROMOLECULES

Dominik J. Green and R. Holland Cheng

*Department of Molecular and Cellular Biology,
University of California Davis*

7.1. THE TRANSMISSION ELECTRON MICROSCOPE

The Transmission Electron Microscope (TEM) is an electron-based imaging system used to reveal the atomic or molecular details of a specimen. High-energy electrons are used to probe the object in question, resulting in the generation of a two-dimensional (2D) image of the object's three-dimensional (3D) information. The electrons in use, with typical energies of greater than 100 kV, have wavelengths less than a tenth of an Ångström, theoretically allowing for imaging resolution far below the sub-Ångström range. However, due to the presence of imperfect imaging conditions such as lens aberrations and sample irradiation, the information transferred from biological specimens via TEM has yet to reach the sub-Ångström limit.

The electrons used for TEM imaging are generated at the top of the EM column by a variety of methods. Early electron microscopes utilized a tungsten filament as an affordable electron source. By heating the filament to high temperatures (2700 K), electrons of the desired energy can be generated and sent down the column. The development of lanthanum hexaboride (LaB_6) crystals was an improvement over the use of tungsten, as its lower work function of 2.5 eV (vs. 4.5 eV), and its magnitude increase in brightness (current density per unit emission angle) allowed for much better beam generation. Unfortunately, thermionic filament sources such as tungsten and LaB_6 share the common limitation of having high electron energy spreads (1.5–3.0

Address correspondence to R. Holland Cheng, Department of Molecular & Cellular Biology, 007 Briggs, CBS, University of California Davis, Davis, California 95616-8536, USA, 530 752-5659, <rhch@ucdavis.edu>.

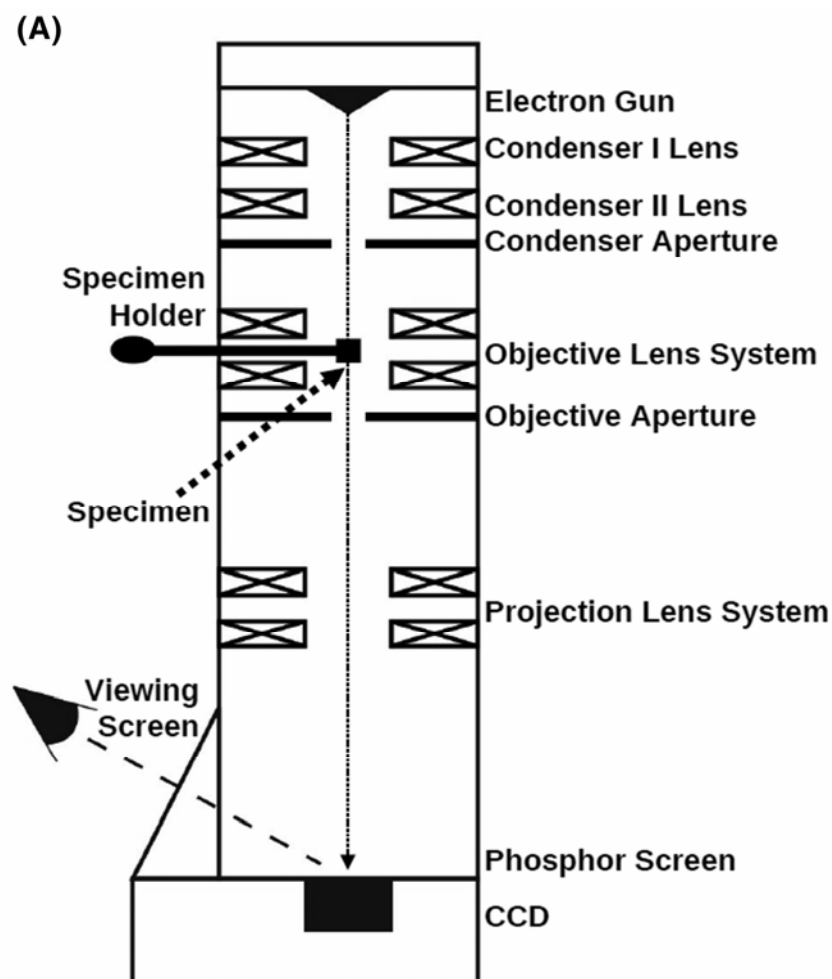
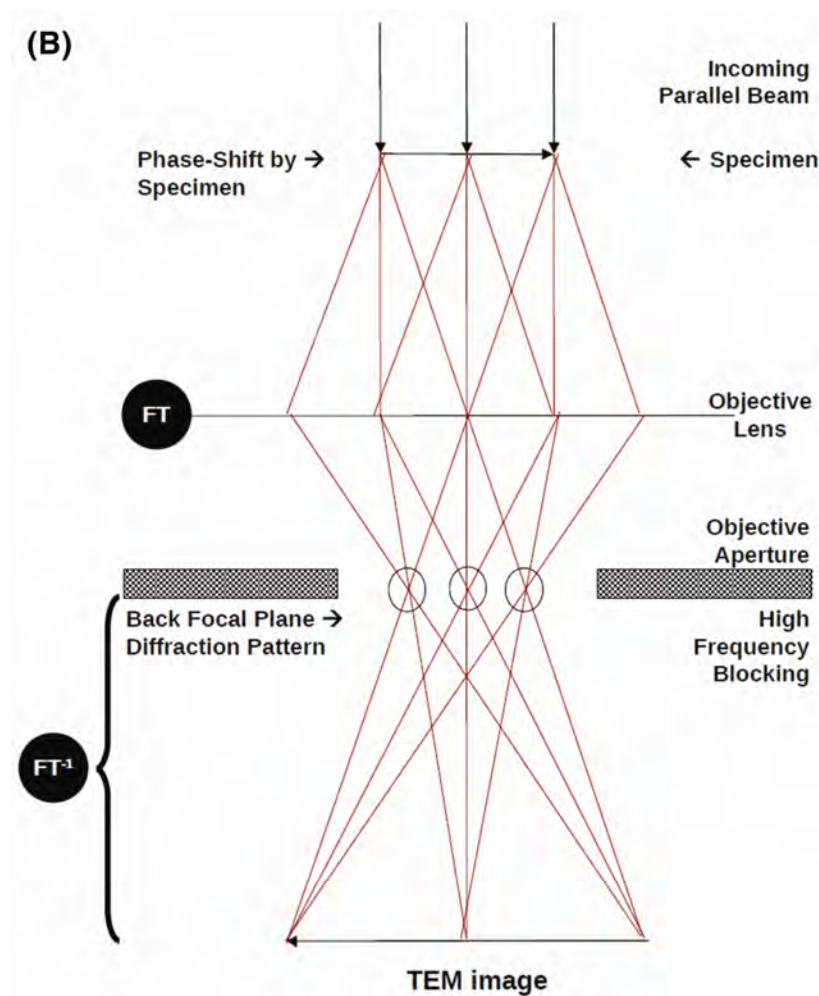


Figure 7.1. Schematic cross-section diagram and effect of lenses on the electron beam in TEM. (A) The electron beam generated from the gun passes through a series of lenses and apertures, as well as the specimen, before a magnified image is formed by striking a phosphorescent screen or charged-coupled device (CCD). (B) (facing page) Image formation in a lens can be described as a double-diffraction process. Incoming parallel beams interact with the sample and undergo a corresponding phase shift. These phase-shifted electrons are then focused by the objective lens and screened by the objective aperture. The objective lens generates an optical Fourier transform of the specimen, which can be seen as a diffraction pattern at the back focal plane. Subsequent lenses perform an inverse Fourier transform of the diffraction pattern, producing a magnified image of the specimen. Please visit www.springer.com/978-1-60327-232-2 to view a high-resolution full-color version of this illustration.

eV), which will eventually contribute to chromatic aberration with the lens system. The modern TEMs are equipped with a field emission gun (FEG), which generates extremely bright (1000 times greater than tungsten or LaB₆) and low-energy spread (0.3 eV) electrons through the application of an extraction voltage at the cathode tip under ultrahigh vacuum. Usage of FEGs has



risen considerably since their introduction, as the highly coherent electrons that are produced allow for the highest possible resolution. Its main drawback, however, is a requirement for vacuums of less than 10^{-8} Pa, which can be expensive to generate.

After electrons are generated, they must be sent down the column to impinge upon the sample. Along the length of the column, various magnetic lens systems are used to focus the electrons (Fig. 7.1A). The first of these systems is the condenser lens system, which determines the physical size of the beam as it impinges upon the specimen, as well as the beam's angular convergence, which affects the coherence of the electrons. Typically, the condenser lens system is composed of two lenses: the first lens, Condenser I, demagnifies the image of the source, while the second lens, Condenser II, controls the beam spot size and angular convergence. A condenser aperture may be used to screen out highly divergent source electrons from sample interaction.

The next set of lenses comprises the objective lens system and is positioned around the specimen. The objective lenses are the most important lenses in the EM, as they are responsible

for image formation of the specimen. Image formation, according to Abbe's theory, is a two-stage, double-diffraction process (Fig. 7.1B). That is, an image is the diffraction pattern of the diffraction pattern of an object. In the first stage of image formation, a parallel beam of rays incident on the object is scattered and the interference (diffraction) pattern is brought to focus at the back focal plane (BFP) of the lens. This stage is sometimes referred to as the forward Fourier transformation. A lens, essential for image formation, also acts to focus the diffraction pattern at a finite distance from the object at the BFP of the lens. If the lens is removed from behind the object, no image forms, but instead Fresnel diffraction patterns form at finite distances from the object. The second stage of image formation occurs when the scattered radiation passes beyond the BFP of the lens and recombines to form an image. This stage is often referred to as back or inverse Fourier transformation. Image formation is analogous to Fourier analysis in the first stage, and Fourier synthesis in the second stage. To be discussed further below, Fourier image analysis is a powerful method, as it separates the processing of TEM imaging into two stages, where the transform may be manipulated and back-transformed similarly in the second stage to generate a noise-filtered image in the subsequent analysis [1].

Due to the current limitation of magnetic lenses, the objective lenses are responsible for most of the aberrations present in the EM, so its design during engineering and operation during imaging must be carefully optimized to limit these effects. The electrons that pass through the sample can be screened out using an objective aperture located at the BFP. Removal of electrons by the condenser aperture functions as a lowpass filter by blocking out high-angle scattering. The contrast that is generated in an EM image as a result of blocking out these scattered electrons is known as amplitude contrast. Contrast from the EM may also be generated via phase contrast. Such contrast is generated by electrons that are phase shifted due to elastic interactions within the specimen. Phase contrast contributes significantly less in the image than does amplitude contrast, but its effects can be varied in a spatial frequency-dependent manner through the intentional introduction of imaging defocus through the objective lens. Usage of TEM for biological sample analysis primarily operates through phase contrast and will be discussed more below.

The effects of aberrations due to the objective lens can severely limit the attainable resolution of an EM. Due to the differential focusing of electrons along the length of the objective lens, spherical aberrations result, turning the point source of the focused beam into a finite-sized disc (disc of least confusion; Fig. 7.2). This effect is purely a consequence of the imperfect functionality of the objective lens and cannot be eliminated. However, its negative effects may be reduced by the addition of a spherical aberration corrector into the column, which compensates for differential focusing. Additionally, electrons that arrive at the objective lens with different energies will experience different amounts of focus, resulting in chromatic aberration. Thermionic electron sources generate electrons with sufficiently large energy spreads that lead to chromatic aberration. Notably, the effect has been drastically reduced with the introduction of the aforementioned FEG electron sources, which are able to generate electrons with a much narrower energy range. With an FEG electron source, chromatic aberration is no longer a resolution-limiting factor in biological TEM. A final aberration introduced by the objective lens results from non-isotropic focusing effects and is termed astigmatism. The presence of astigmatic focusing results in the unequal emphasis of spatial frequencies in a direction-dependent manner. An astigmatism can be compensated for by introduction of astigmatic correctors positioned after the objective lens, which are able to restore the correct roundness of the electron beam.

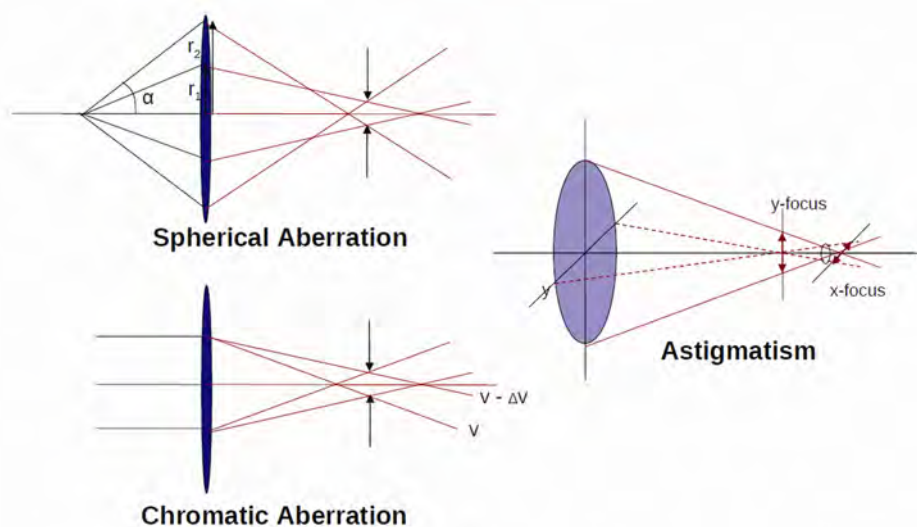


Figure 7.2. Schematic of the aberrations contributed by the objective lens. (A) Differential focusing of the electrons by the lens along its diameter results in spherical aberration. (B) Similarly, differential focusing of electrons of varying energies generates a chromatic aberration. (C) Finally, non-isotropic directional focusing leads to astigmatic effects. Please visit www.springer.com/978-1-60327-232-2 to view a high-resolution full-color version of this illustration.

The projector lens system comprises the final lens system of the TEM. The goal of these lenses is to perform any necessary magnifications of the specimen and to project the final image of the specimen onto the imaging screen or collection device. To allow for visualization of the electrons, the imaging screen is coated with a phosphorescent compound that emits faint green photons when struck by the impinging beam. To record an image of the specimen, either photographic film or a charged-coupled device (CCD) can be used. The film or CCD is located beneath the imaging screen, and the amount of beam exposure to these elements can be controlled to allow for optimal exposure times.

The operation of a TEM requires high vacuum conditions. For thermionic electron sources vacuums of 10^{-2} – 10^{-4} Pa are required, and as stated previously, 10^{-8} Pa is required for FEG sources in order to keep the FEG cathode free from any molecular contamination. Additionally, any gaseous molecules present within the column are free to interact with the electron beam, so minimizing their presence decreases the likelihood of spurious electron scattering by non-specimen atoms. Significant amounts of time can be lost in order to generate the vacuum pressures necessary for TEM operation, so it is important to work extremely carefully during specimen loading and removal to prevent vacuum failure.

To image the specimen, it must first somehow be positioned within the path of the beam and within the polepiece of the objective lens. Microscopes are available that allow for either top or side entry of the specimen into the EM column. Side-entry columns are most commonly used and allow for tilting of the specimen; however, they also tend to be less mechanically and temperature stable than the top-loading columns. For side-entry columns the specimens are loaded onto metal grids (usually copper or nickel) and are placed into a specimen holder. The holder is then inserted directly into the column perpendicular to the beam path. Top-loading

columns place the specimen grid into a mechanical holder that gets lowered down into the EM column along the beam axis. In both scenarios, the height of the specimen relative to the objective lenses must be accurately calibrated for optimal imaging.



Figure 7.3. Schematic of the incoming and outgoing electron wave fronts during imaging. The incoming electrons can be approximated as a planar wave with constant phase. Upon interaction with the sample, the transmitted wave experiences a phase shift relative to its incoming phase, generating phase-based contrast.

7.2. PHASE-CONTRAST IMAGING

The electron beam that impinges upon the sample can be approximated by the following wave equation, with x being the 2D vector corresponding to position in space, k_0 the wave momentum vector, and z the particular plane in the direction of the incident wave (Fig. 7.3):

$$\psi_{\text{incident}}(x) = \exp^{ik_0 \cdot z},$$

As the electrons pass through the sample and interact with its force potentials, they experience a phase shift of $e^{i\eta(x)}$ relative to non-interacting electrons, giving a wave transmission modeled by

$$\psi_{\text{transmitted}}(x) = \exp^{i\eta(x)} \exp^{ik_0 \cdot z}.$$

The phase shift experienced by the passing electrons is influenced by the atomic composition of the specimen. The intensity of the diffracted beam can be approximated as the squared magnitude of the object's structure factor, F_k , given by (with f_i the atomic scattering power or atomic form factor and r_i the position of an atom within the object)

$$F_k = \sum_i f_i \exp^{-2\pi i k \cdot r_i}.$$

Atoms with larger nuclei will have larger atomic form factors, which allows them to scatter electrons to a greater degree. Lighter elements present within biological materials will therefore scatter electrons significantly less than the heavier elements found within non-organic materials.

The superposition of the phase-shifted or scattered electrons with the non-phase-shifted or unscattered electrons generates an image with amplitude contrast. Contrary to conventional light microscopy, imaging of biological samples within the TEM is not performed at focus but rather with varying amounts of underfocus or defocus. As will be discussed in the next section, the

intentional introduction of defocus can emphasize or deemphasize specific features of the specimen in a frequency-dependent manner. Relating to phase contrast microscopy, biological macromolecules are treated as what is termed “weak phase objects” due to their relatively thin nature (less than tens of nanometers in thickness). Because of their thinness, the electrons that are elastically scattered by the specimen tend to undergo only a *single* scattering event. Increasing the thickness of a sample would increase the probability of the passing electrons interacting multiple times with the sample, causing the weak-phase approximation to be invalid. These multiple scattering events are undesirable in biological TEM because their interactions with the sample are immensely more difficult to quantify.

Finally, what is recorded by the CCD or photographic film is the intensity of the incoming electron wavefront and is given by

$$f(x) = |\psi(x)|^2.$$

7.3. THE CONTRAST TRANSFER FUNCTION

Like all optical systems, the TEM is not a perfect imaging system. Due to the perfected formation of glass lenses, modern non-superresolution optical microscopes are now only diffraction limited. However, for TEM, this is not the case as TEM images come nowhere close to the diffraction limit of the electrons that are used. Instead, resolution is limited by the aberrations imparted by the lens system, the mechanical instability of the microscope, and the functionality of image collection devices. The net effect of these imperfections is the contribution of a point spread function (PSF) during imaging, which manifests itself in real space as a blurring of a point source into an Airy disc, or as a frequency-dependent contrast transfer modulation of the image. Similar to optical microscopy, the image that is generated by the electron beams is a convolution of the object with the PSF of the TEM as shown by the Contrast Transfer Function (CTF) (PSF represented by $h(x)$, CTF by $H(s)$, and $\Psi(s)$ as the FT of the object wave equation):

$$\psi_{\text{object}}(x) * h(x) = \{ \mathcal{F}^{-1} \Psi_{\text{object}}(s) \cdot H(s) \} = \psi_{\text{image}}(x).$$

Alternatively, the FT of the image wave equation can be generated by multiplication of the FT of the object with the microscope CTF as shown:

$$\mathcal{F} \{ \psi_{\text{image}}(x) \} = \Psi_{\text{image}}(s) = \Psi_{\text{object}}(s) \cdot H(s),$$

$$H(s) = A(s)E(s)\gamma(s).$$

The term $A(s)$ describes the high-frequency attenuation of the transmitted wave that is removed through the objective aperture, which functions as a binary frequency-dependent mask at the BFP by allowing only the transmission of spatial frequencies within the aperture opening. The sinusoidal-dependent term of the CTF, $\gamma(s)$, is modulated by the amount of defocus (Δz) applied to the specimen, the wavelength of the electrons used in the imaging (λ), and the amount of spherical aberration that is present due to the objective lens (C_s). Since the electron voltage and spherical aberration are constant during operation, the main contribution of CTF modulation is imparted by the operator of the microscope in the form of image defocus:

$$\gamma(s) = -\sin \left[\frac{\pi}{2} C_s \lambda^3 s^4 + \pi \Delta z \lambda s^2 \right].$$

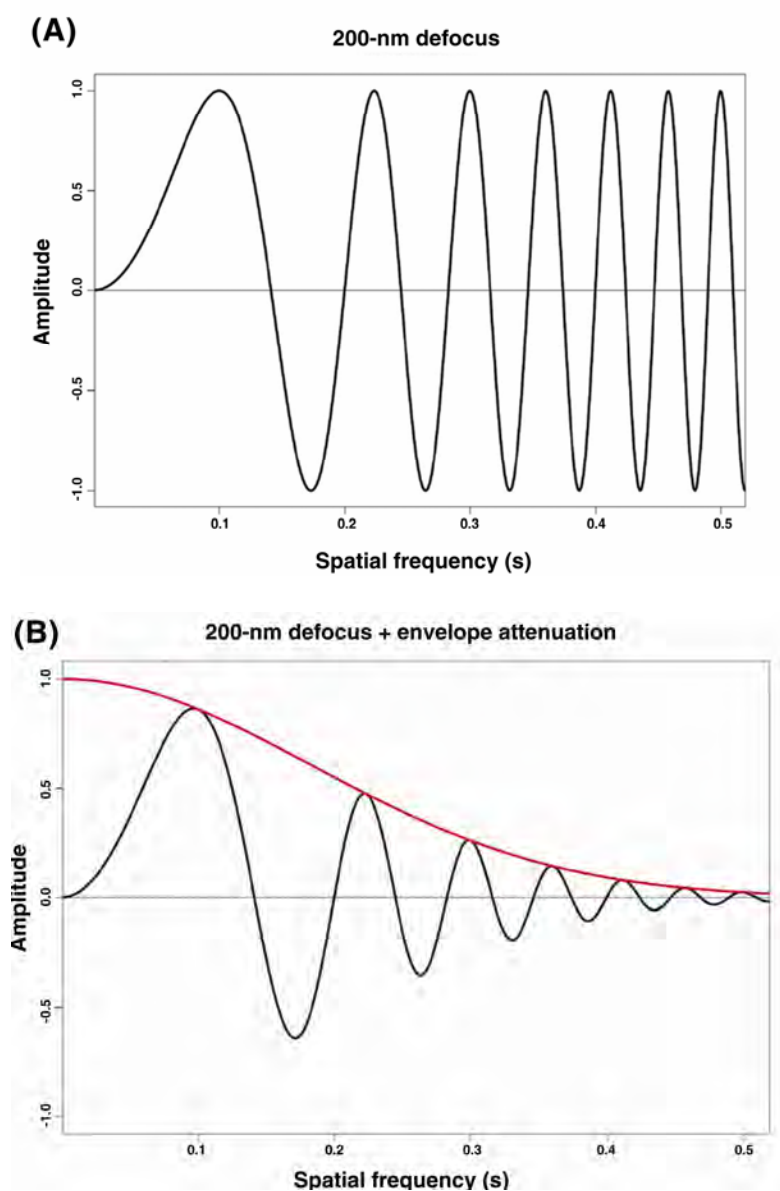
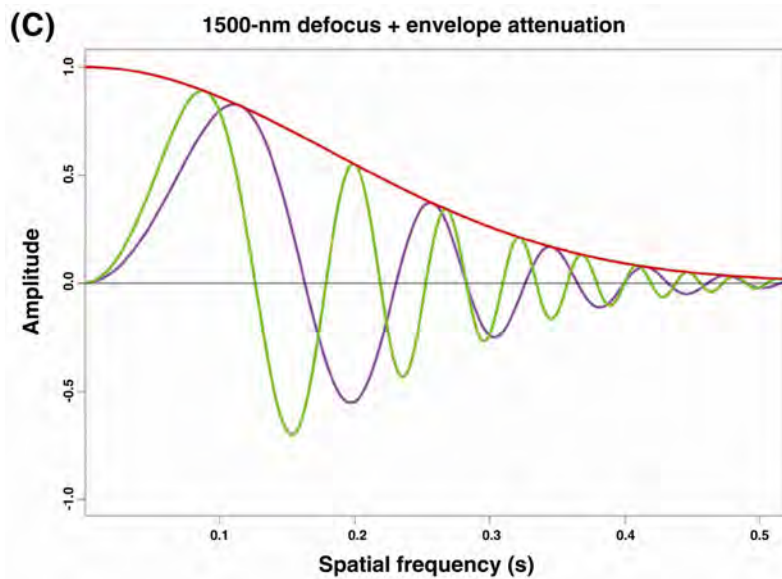
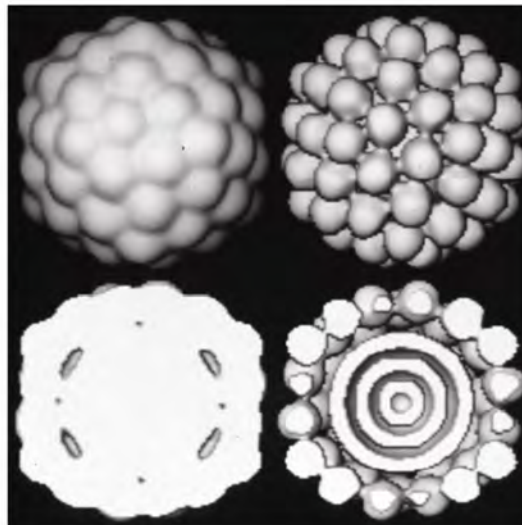


Figure 7.4. Plots of simulated contrast transfer functions (CTFs). (A) CTF at 2000-nm defocus without suppression from an envelope function by having spatial frequency as the variable of the function. (B) Spatial attenuation at high frequencies due to the envelope function. (C) (facing page) CTFs at 1500- (purple) and 2500-nm (green) defocus reveal slower CTF oscillations and a higher point-to-point resolution for the lower defocus and faster CTF oscillations and a lower point-to-point resolution for the higher defocus. Please visit www.springer.com/978-1-60327-232-2 to view a high-resolution full-color version of this illustration.

The net effect of $\gamma(s)$ is a sinusoidal contrast inversion of the object's spatial frequencies. The point-to-point resolution of a TEM is determined by the first zero-crossing of the CTF (Fig. 7.4). Higher amounts of defocus result in a lower point-to-point resolution and impart more



(D)



rapid contrast inversions, whereas lower amounts of defocus lead to greater point-to-point resolution and generate less frequent inversions of contrast. In order to obtain a true image of the specimen, the CTF must be corrected for. Additionally, since particular defocus values have unique zero-crossings where no contrast information is transferred, datasets must be collected across a range of defoci in order to compensate for the lack of information at these spatial frequencies [2,3].

The CTF is also modulated by the TEM's own transfer function, or envelope function, $E(s)$, which can be approximated as a Gaussian falloff of information transfer at higher-spatial frequencies. These effects are due to spherical aberration, $E_s(s)$, chromatic aberration, $E_c(s)$ (which

is dependent upon the chromatic aberration coefficient, C_c , specimen drift, $E_d(s)$, and vibration, $E_v(s)$, as well as detector contributions, $E_D(s)$, and are the limiting factors in TEM resolution:

$$E(s) = E_s(s)E_c(s)E_d(s)E_v(s)E_D(s),$$

$$E_s(s) = \exp\left[-\left(\frac{\pi\theta_0}{\lambda}\right)(C_s\lambda^3s^3 - \Delta z\lambda s)^2\right]$$

$$E_c(s) = \exp\left[-\frac{\pi^2}{4}\left(C_c\frac{\delta E}{E}\right)^2\lambda^2s^4\right].$$

The effect of the envelope transfer function on biological structural analysis therefore requires a great number of sample images to be generated in order to achieve an appreciable amount of information transfer at higher-spatial frequencies.

Since the PSF modulates the actual features of the sample under study in a frequency-dependent manner, it would be desirable to compensate for its effects to obtain a final image that most closely resembles the specimen. As the CTF is the FT of the PSF, it can be divided out in Fourier space if the correct defocus can be determined as follows:

$$\psi_{\text{object}}(s) = \frac{\Psi_{\text{image}}(s)}{H(s)}.$$

In practice, generation of the power spectrum of recorded image intensity can reveal the frequency-dependent oscillations of the CTF. The oscillations within a micrograph will correspond to a unique defocus that can then be used to correct for the CTF in a spatial-frequency-dependent manner (Fig. 7.4). Once the CTF is accounted for, a more accurate interpretation of the specimen can be determined. If the CTF is not corrected during an analysis, one can expect the effective point-to-point resolution of the data to be reliable only to the first zero-crossing of the CTF.

7.4. THE PROJECTION THEOREM AND SINGLE-PARTICLE RECONSTRUCTION

The goal of single particle reconstruction (SPR) is to determine the 3D structure of a desired biological macromolecule from a set of its 2D projections. To reconstruct a 3D structure from a 2D projection set, the Projection Theorem comes into play (Fig. 7.5). This theorem states that an arrangement of the 2D FTs of various 2D real-space projections of an object can be oriented and combined in 3D Fourier space, wherein a subsequent back Fourier transform (FT^{-1}) of the 3D Fourier information can generate a 3D representation of the original object in real space. Usage of the TEM automatically generates the 2D projections required by the projection theorem. The determination of the orientation of each projection and their summed conversion into a 3D model are performed computationally through a variety of related algorithms. The orientation of a particular projection or class average is determined by five parameters: two Cartesian centers, x and y , and three Euler rotations, out-of-plane θ and ϕ , and in-plane ψ . Depending on the reconstruction algorithm that is used, the order of parameter determination can vary and even may involve determination of all five parameters simultaneously [4–6].

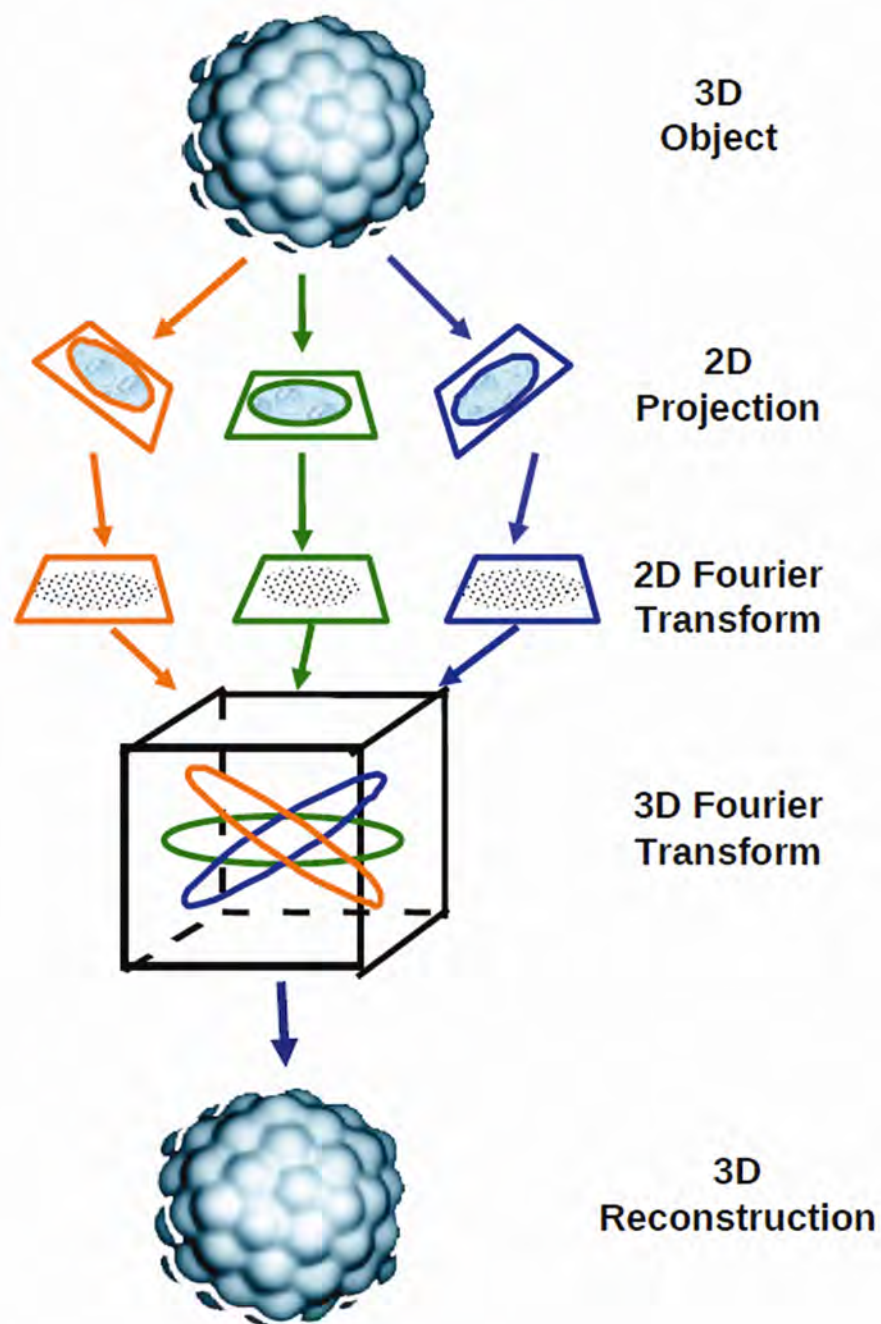


Figure 7.5. Projection theorem at a glance. A 3D object is imaged via TEM in varying orientations, generating 2D projections of itself. FTs of the 2D projections are oriented relative to one another in 3D Fourier space, followed by a Fourier back transform that regenerates a representation of the starting object. Please visit www.springer.com/978-1-60327-232-2 to view a high-resolution full-color version of this illustration.

Due to the low signal-to-noise ratios (SNRs) present in TEM and the fact that 3D information is superimposed into a 2D projection, the usage of a single projection image is insufficient to obtain an accurate 3D representation of a macromolecule. To overcome these problems, multiple projection images with known orientations must be combined to generate a more accurate 3D representation. If enough particles are used, the SNR of the higher-spatial frequency terms is increased and higher-resolution structures can be attained. Additionally, by ensuring that the projection images are randomly oriented, all regions of Fourier space can be adequately filled for accurate reconstruction back into a real-space volume. If projections of particular views are not included in a reconstruction process, then their corresponding spatial frequencies in Fourier space will be missing and the real space reconstruction will suffer as a result. Such an occurrence is common in tomography, where tilt angle limitations generate a missing wedge or cone in Fourier space but can be minimized in SPR by ensuring that all possible projected orientations are present in the reconstruction process. As just stated, single-particle reconstruction does not rely on a *single, lone* molecule to determine a structure, but rather a collection of *isolated, identical* molecules.

7.5. ADVANTAGES OF SPR OVER X-RAY CRYSTALLOGRAPHY

SPR was developed as a means to study proteins and protein complexes that were not amenable to study via X-ray diffraction (XRD) techniques. The first requirement for XRD is a suitable 3D crystal of a purified protein. Generation of these crystals is often the limiting step in structure determination, and for many proteins, crystals may be unable to form, too small for analysis, or unable to diffract to an appreciable resolution. Due to the ability of the EM to visually identify individual protein complexes, 3D crystals do not need to be grown. By taking an individual biomacromolecule and averaging various projections together in an orientation-dependent manner, SPR is able to sidestep the requirement for an ordered array of protein. Another significant advantage related to this is the fact that SPR is able to analyze heterogeneous metastable complexes. Whereas a crystal used for XRD usually contains a highly stabilized macromolecule in a fragile packing arrangement, SPR allows proteins to easily exist in a variety of conformations. It is therefore easy to image samples using EM with a wide range of substrate and buffer conditions that are not amenable to particular crystal analyses. A common problem frequently encountered by crystallography is the growth of crystals of large macromolecular complexes. Such complexes have immense amounts of surface area that often are not capable of forming favorable crystal contacts. Additionally, these complexes tend to be somewhat fragile and can easily dissociate into subcomplexes during the crystallization process. SPR is able to handle such large complexes, again by treating them as individual components in the data-collection and structural-refinement process. Another potential drawback of crystallography is the influence of crystal packing upon protein structure. Not only are the crystallized proteins present in only a partially hydrated environment, they also exhibit crystal contacts that may not be indicative of their structure while free in solution. These hydration and crystal packing effects are not present in SPR because the protein complexes can be imaged in a completely hydrated environment and outside of the crystal context. A final strength of SPR over crystallography is the amount of pure protein that is required for a structural analysis. Usage of SPR can determine the structure of macromolecules with as little as 0.5 mg/mL of sample, whereas some crystal

growth conditions can require as much as 10–30 mg/mL of purified sample. Additionally, the protein preps for SPR can contain modest levels of background impurities as their low molecular weights will only contribute to background signal, whereas similar background contamination in crystallization attempts can prevent successful crystal growth [2,7].

However, SPR does have drawbacks when compared to XRD. First and foremost is the resolution limit on SPR due to SNR attenuation at higher-spatial frequencies. For high-resolution structures to be generated, thousands to tens of thousands of images need to be averaged together, which requires significant computational effort. XRD does not have this problem and is able to achieve high resolution because of the SNR-amplifying effect of an ordered crystal. Additionally, limitations on the attainable resolution of imaging data from biological samples has yet to pass the 3.5-Å barrier, keeping it significantly behind the sub-Ångström resolution capability of XRD. Finally, there is a size limitation on SPR usage. Currently, the smallest structures solved to date (and only to a very modest resolution) have been on the order of 150–250 kDa. Structures with molecular weights smaller than this do not have enough mass to generate significant electron scattering events, making them nearly invisible above background image levels.

7.6. SAMPLE PREPARATION

To generate data suitable for SPR, the macromolecule under study must be prepared in a suitable fashion. Any purified protein, whether produced through recombinant means or purified directly, can be suitable for SPR if it is relatively homogeneous in composition. Significant amounts of contaminating background proteins with sizes similar to the sample under study can interfere with the reconstruction process if they are not removed prior to imaging. It is therefore advisable to run protein preparations through multiple purification columns to ensure the removal of contaminants similar in shape or size. Additionally, high levels of salt, glycerol, or other cryoprotectants will result in the degradation of image quality due to their interaction with the electrons, so dialysis may be required to reduce their concentrations when these compounds are present [1,8].

Several preparation techniques are used to image macromolecules within the EM. The most common practice is negative staining and involves the use of heavy metal salts such as uranyl acetate, lead citrate, or ammonium molybdate to generate contrast. Briefly, the sample is applied to a carbon-coated EM grid and blotted dry. The negative stain is then applied to the sample-containing grid and is blotted dry as well. The metal salts orient themselves around the periphery of the sample, providing a high-contrast surface detail of the specimen. Electrons more prevalently interact with the stain's heavy metal atoms due to their larger scattering cross-section than with the lower atomic mass atoms within the biological specimen, causing a greater degree of contrast enhancement compared to a biological sample alone. Although use of negative stain can provide high-contrast images, surface tension effects upon blotting/drying can lead to distortions of the sample that alter its true structure. Also, since the negative stain particles are of finite size, they do not always penetrate into the cavities or crevices of biological macromolecules, leaving these structural features irresolvable in the final image. Recent techniques have involved embedding the biological sample within an intact layer of heavy metal salts. Such stain-embedding techniques have the advantage of high image contrast but are able

to circumvent most of the effects of particle distortion due to drying. The most significant development in sample preparation, however, has involved the embedding of sample within a thin-layer amorphous ice instead of metal salts. Such attempts are able to successfully preserve the native water-like environment of the biological sample and do not suffer from the distortion artifacts of negative staining. By placing the sample onto a grid coated with holey carbon, the specimen is able to migrate into a meniscus-like layer of water within the carbon holes. Rapid plunging of the sample into a cryogen with a high specific heat capacity such as liquid ethane causes the water to freeze rapidly enough to prevent an ordered water phase from forming, which would distort the sample's liquid environment and potentially alter its native structure. The sample can then be kept at extremely low "cryo" conditions during data collection with specialized liquid nitrogen-cooled cryoholders. The process of freezing and imaging a frozen biological sample is collectively known as cryo-electron microscopy (cryoEM) and is currently the gold-standard in SPR for native, high-resolution structure determination.

7.7. IMAGING CONDITIONS

The energy of the electrons imparted to a biological sample are immense and are enough to quickly destroy the specimen before adequate data can be collected. To help reduce the effects of electron beam-induced damage, the EM must be operated in a manner that reduces the total dose of electrons that impinge upon the sample. Common techniques involve reduction of either beam brightness or beam spot sizes, which limit the number of electrons that reach the sample. Exposures of $15\text{--}25\text{ e}^-/\text{\AA}^2$ are enough to alter the physical and chemical structure of a biological specimen, so reducing the amount of electron exposure to $5\text{--}10\text{ e}^-/\text{\AA}^2$ is desirable. However, such reduced beam exposure drastically affects the contrast in the resulting image, which has a pronounced effect on the ability to detect a particle above background due to the extremely low image SNR across all spatial frequencies. Development of cryoEM techniques revealed the preserving nature of imaging at liquid nitrogen temperatures, allowing the frozen specimen to tolerate a modest amount of sample radiation before becoming irreversibly damaged. As previously stated, the use of cryoEM requires specialized specimen holders that can accommodate a cryogen such as liquid nitrogen, which serves to keep the specimen frozen throughout image collection. Additionally, anti-contaminator blades may be placed within the EM column surrounding the specimen in order to adsorb stray gaseous water molecules present in the column. The readsorption and subsequent freezing of water molecules onto an extremely cold grid can generate cubic or hexagonal ice crystals that can hinder optimal data collection. Recent advances in cryoEM have involved the use of liquid helium as a cryogen, with purported increases in radiation damage over that of liquid nitrogen.

7.8. DATA VALIDATION

Once micrographs (film or CCD datasets) have been collected for use in SPR, they must be checked for quality. By computing the power spectrum of a micrograph either with an optical diffractometer or via a computerized fast Fourier transform, one is able to determine if any specimen drift has occurred, and if astigmatism or charging effects are present. Specimen drift is the result of mechanical instability of the specimen holder during image recording. It can be

easily characterized by the directional absences of CTF oscillations (also called Thon rings) in the direction of drift. Astigmatism can be identified by elliptical Thon rings present in the power spectrum, indicating a direction-dependent difference in focus in the micrograph. Charging effects occur when localized charges are present on the specimen or grid. These charges are able to interact with the electron beam, generating direction-independent imaging artifacts. Micrographs that exhibit any of these three phenomena should not be used in subsequent structural analysis. Additionally, by looking at the extent of the Thon rings present within a power spectrum, one is able to determine a lower-level estimate of the resolution limit of a particular micrograph. As imaging conditions are perfected, a skilled electron microscopist will be able to maximize the number of Thon rings present within a power spectrum. The more Thon rings that are present, the further out in reciprocal space useful information has been transferred on that micrograph, indicating higher-resolution content [9,10].

7.9. DATA SELECTION & PREPARATION

SPR requires the extraction of a single-protein complex for structural elucidation. To perform this, the user must either interactively box out desired macromolecule image projections from a micrograph or automatically extract the images computationally. Interactive boxing is an extremely time-consuming process, but it may be necessary for highly heterogeneous preparations or if automated boxing has proven unsuccessful. A benefit of manual particle selection is that it allows the user to get familiar with orientations or heterogeneity present in the dataset that would not happen with automatic particle selection. Many techniques have been developed to perform automated particle selection, ranging from correlation-based boxing from a reference dataset to neural network-based boxing refinement. Depending on the size of the molecule present and the quality of the data, automatic boxing may or may not be a viable option for particle selection [11].

Once the particles required for analysis have been selected, they are usually masked along their periphery to remove any unwanted background signal. It is also desirable to apply a real space- or Fourier space-based filter to the selected images. A particularly effective frequency-based filter used in many SPR experiments is the bandpass filter. The bandpass filter applies both a highpass filter to remove any low-resolution background ramping that is commonly found in images and a lowpass filter to remove high-resolution noise components that may negatively bias the reconstruction process. Systematic extension of the lowpass filter to subsequently higher and higher-spatial frequencies can be performed to slowly provide the refinement process with increasing amounts of higher-resolution features for later stages of image alignment (Fig. 7.6). Other filters used in SPR include median, wavelet, and bilateral filters, the use of which depend on the desired filtering characteristics.

7.10. MULTIVARIATE STATISTICAL ANALYSIS

Once the particle images have been preprocessed, it is beneficial to perform a preliminary analysis to familiarize oneself with the data. Individual particle images contain extremely low SNRs, so the amount of information one can glean from them is very limited. However, by

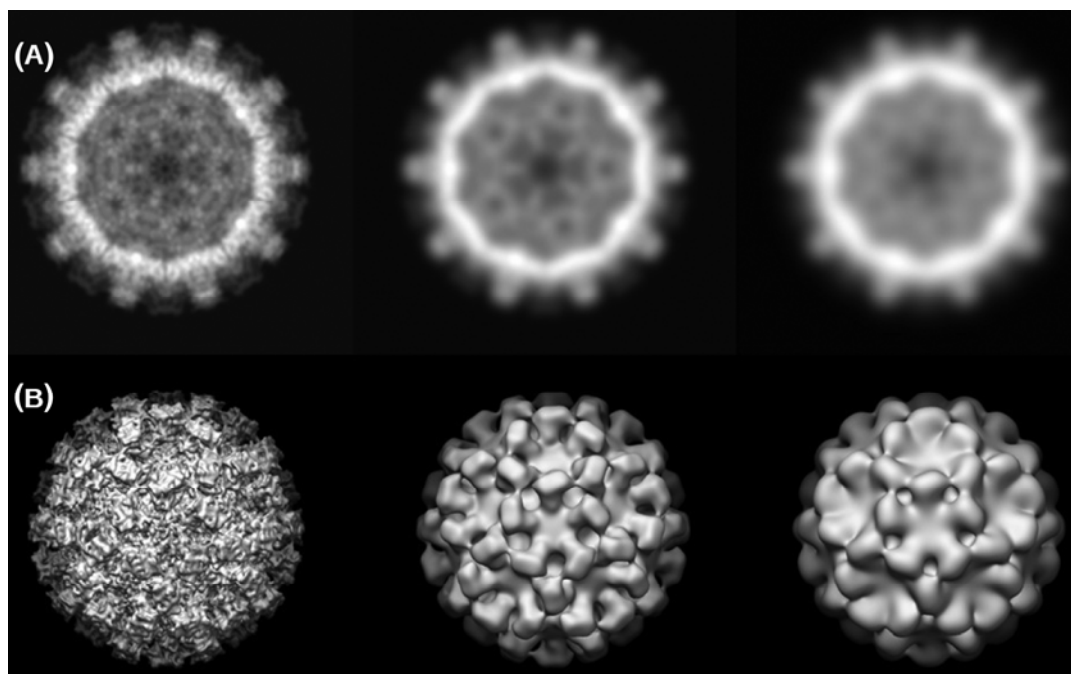


Figure 7.6. The effect of lowpass filtration. (A) 2D reprojections down the 5-fold axis of Norwalk virus (1IHM). (B) 3D surface renderings of Norwalk virus. Lowpass filters of spatial frequency $1/(10 \text{ \AA})$ (Column #1), $1/(30 \text{ \AA})$ (Column #2), and $1/(50 \text{ \AA})$ (Column #3). Structural detail is gradually lost as the lowpass filter is extended to lower spatial frequencies.

grouping together similar particles (based on projection orientation or conformational orientation), the SNR of those particular views can be increased, allowing more meaningful structural details to become apparent (Fig. 7.7). Statistical methods such as multivariate statistical analysis (MSA) have been devised in order to analyze the variation present within an image dataset. Variation can relate to a number of factors, including the variation present due to differences in the projection orientation dataset and conformational variation due to component variability or structural flexibility.

The overall goal of MSA is dimension reduction of the dataset and is accomplished by determining the fewest number of components required to describe the dataset as a whole. This operation is performed by determining the eigenvectors of the covariance matrix from vectorial representations of all projection images. By analyzing the eigenvectors that result, unique contributors of variance within the dataset can be identified and can be subsequently used for classification. Linear combination of the various eigenvectors with one another can be performed, resulting in an accurate approximation of the original dataset. Through MSA application, instead of representing the full dataset as an array of hundreds to thousands of images each with tens of thousands of pixel components, it can now be interpreted as a linear combination of a very small subset of eigenvectors and a datafile that describes the relative contribution of each eigenvector to the original images.

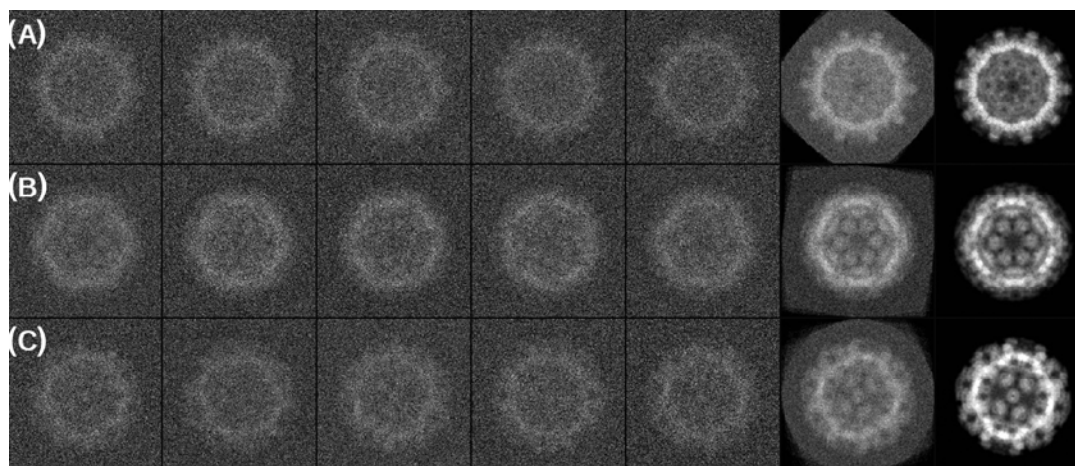


Figure 7.7. Classification of orientation subsets of Norwalk virus reprojections. Orientation of the reprojections corresponding to (A) 5-fold, (B) 3-fold, and (C) 2-fold axes. Columns 1–5 are noisy representations with random in-plane rotations of their particular class. Column 6 corresponds to the aligned average of the particles in columns 1–5. Column 7 is a reprojection of a Norwalk virus model in a corresponding orientation to column 6. The class averages in column 6 reveal much more structural information than the individual images in columns 1–5 and bear a strong resemblance to their parent reprojection in column 7.

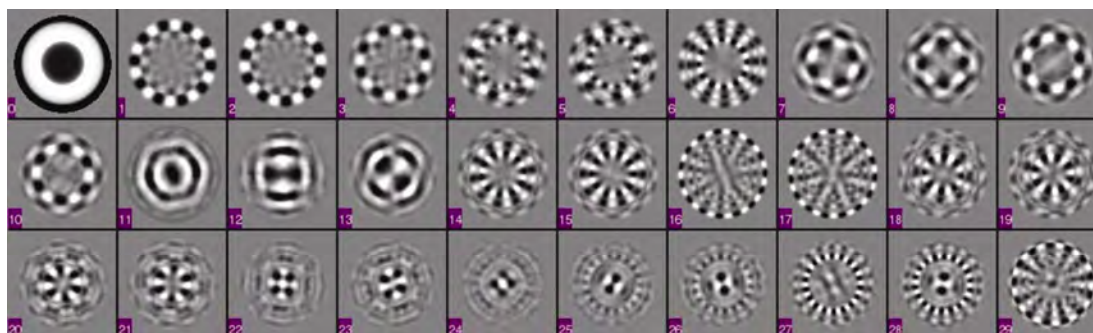


Figure 7.8. First thirty eigenimages generated from a mock dataset of reprojected lumazine synthase capsids lowpass filtered to 5 Å. The first eigenimage corresponds to the center of mass of the full datacloud and represents the average of the dataset. The early eigenimages reveal lower-order symmetry modulations, while subsequent ones reveal higher-order symmetry modulations that characterize finer capsid details. Please visit www.springer.com/978-1-60327-232-2 to view a high-resolution full-color version of this illustration.

The eigenvectors that are determined by MSA can be directly interpreted as eigenimages (images that are pictorial representations of the eigenvectors; Fig. 7.8). By analyzing the variations present within the dataset in a visual manner, one may be able to better understand inherent differences within the dataset as a whole. As the eigenvectors are determined, the most predominant variations within the dataset are found to exhibit the highest eigenvalues. The higher an eigenvector's eigenvalue, the more variation that particular eigenvector describes within the

whole of the dataset. The most significant eigenvectors within SPR data tend to characterize low-frequency structural modulations. These include the orientation of the macromolecule, its overall shape and size, symmetry arrangements, and large-scale structural variations such as changes in subunit binding stoichiometry or large protein domain movements. Less significant eigenvectors tend to have smaller eigenvalues but are useful in specifying higher-frequency modulations present in the data such as small-scale structural rearrangements and fine changes in adjacent orientation parameters. The least significant eigenvectors contain the lowest eigenvalues and tend to describe the noise present within the data. These eigenvectors are not useful in describing actual variations present within the images and can be disregarded during eigenanalysis [12].

7.11. CLASSIFICATION

As mentioned above, classification of individual image projections based on similarity is a powerful technique used to overcome the inherently low SNR present in TEM datasets. Classification can be performed in two different manners: unsupervised or supervised. Unsupervised or reference-free classification classifies images within a dataset without the use of outside references, while supervised or non-reference-free classification classifies the images with respect to outside references [13,14].

Unsupervised classification is a computationally intensive technique, as it seeks to find relations between images with zero outside guidance. Classical techniques for performing unsupervised classification involve K -means clustering and Hierarchical Ascendant Classification (HAC). Both of these techniques require previous application of MSA and eigenvector generation before being performed. By analyzing the distribution of images in multidimensional eigenspace performed by MSA, K -means and HAC are able to classify similar images with one another in an eigenvector-dependent fashion. K -means clustering is accomplished by placing a set number of seed class markers into the eigenspace datacloud (Fig. 7.9). These seeds correspond to gravity centers of individual image classes. With each iteration, new classes are generated by migrating the gravity centers closer to the centers of clustered images within the datacloud. K -means clustering is limited due to the fact that the location of starting class seeds can greatly influence the final classification results. HAC is performed by successively grouping like images together until a certain classification threshold is reached. To perform the grouping, HAC through Ward's criterion seeks to maximize the interclass variance (variance between different classes) while minimizing the intraclass variance (variance within a single class). Doing so helps to encourage the formation of classes that are quite dissimilar from one another but are made up of individual images that are very alike. Non-reference-based classes can also be generated through the use of Self-Organizing Maps (SOMs). An SOM implements dual-layer neural networks to iteratively classify molecules according to similarity, in addition to providing a 2D layout that indicates which classes are most similar to one another. Classes adjacent to one another on an SOM are most similar to one another, while classes found at the corners of the layout tend to represent extrema of the classified variability.

With supervised classification, images within a dataset are not compared to one another but instead are compared to a reference dataset. Performance of reference-based classification is

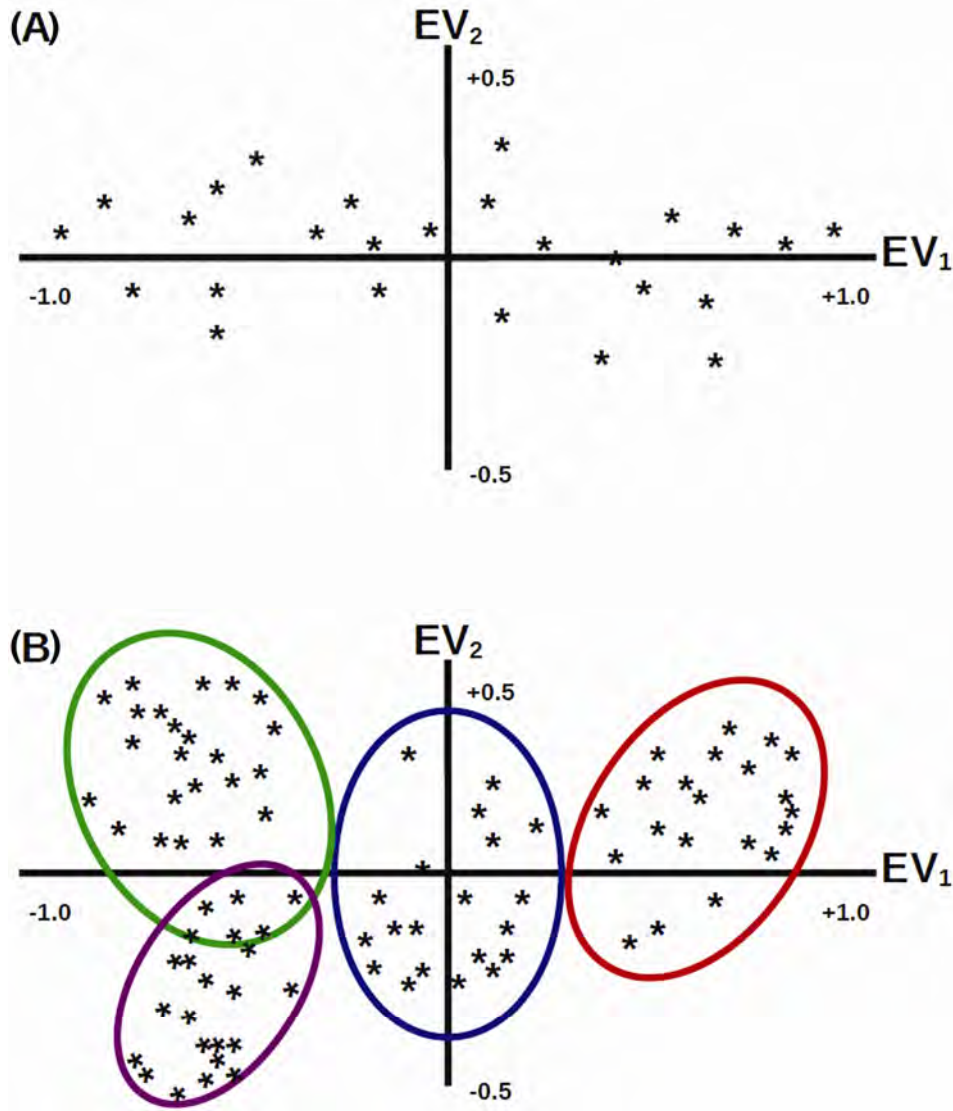


Figure 7.9. Images distribution of in multidimensional eigenspace. (A) Example of a 2D projection of image vectors in eigenspace onto the first and second eigenvectors. Principal variation occurs across eigenvector 1, with eigenvalues spanning from -1 to $+1$. Less variation is seen along the direction of eigenvector 2, with eigenvalues only ranging from -0.5 to $+0.5$. (B) Classification of a dataset projected onto the first and second eigenvectors, as determined by *K*-means clustering. Images within a class share similar eigenvalues with one another across both eigenvectors and can be grouped into nearly homogeneous classes. The classes in green and purple show some overlap, as there is not a complete distinction between them based solely on two eigenvectors. Please visit www.springer.com/978-1-60327-232-2 to view a high-resolution full-color version of this illustration.

less computationally demanding than non-reference-based classification as class seeds are already generated and do not need to be artificially derived through iterative procedures. The main drawback of supervised classification, however, is the bias that is introduced by the refer-

ence projections. The classification of an input dataset will be guided by the references, and if there is a significant difference between the data and reference datasets, inaccurate or inconsistent classification may result. Despite this limitation, reference-based classification is a powerful technique for use in refinement cycles as proper reference projections can effectively seed the classification of projection images that are limited in popular number and would not likely arise in unsupervised techniques.

7.12. ANGULAR RECONSTITUTION

In the method of angular reconstitution, particles are grouped into related class averages via MSA and subsequent classification. To determine the orientation of the class averages relative to one another, angular reconstitution is performed. This method relies on the determination of common projection lines that are found from 2D Radon transforms by comparing all generated class averages against one another (Fig. 7.10). By iteratively refining the orientations determined for each class average with the goal of minimizing the orientation error across all classes, a reliable 3D model can be generated [15].

7.13. REFERENCE-BASED REFINEMENT

Reference-based refinement is a powerful technique that can be used to determine the structure of a macromolecule. To start, a set of reference projections is generated from an initial starting model that is projected across an asymmetric unit (Fig. 7.11). The images within the dataset are then compared to the set of reference projections in order to determine their relative orientations. Once the orientation of each image has been determined, a 3D model can be generated. This procedure is iterated until no further changes occur within the outputted volumes between iterations.

The most common flavor of reference-based refinement used in SPR involves the classification of individual projection images to a particular reference projection. All particles assigned to a specific reference orientation are aligned to one another and then averaged, generating a class average for that particular orientation. Noise-reduced class averages for each reference projection result are subsequently used to generate a 3D model. A variation on this theme exists that involves the generation of class averages *before* comparison to reference projections. Here, signal-strengthened class averages can be very accurately correlated to a reference, as opposed to correlation with a noise-weakened individual projection. A final variation avoids the usage of class averages altogether. In this case, individual images are assigned an orientation through reference matching, and are then directly used to generate a volume.

The correlations used to determine the level of matching between the image dataset and reference projections are extremely varied and depend upon the single-particle reconstruction package in use. Some packages use direct real-space correlations between the images, while others rely on Fourier space-based metrics. The Polar Fourier Transform (PFT) is noteworthy for its use in spherically symmetric objects such as viral capsids. The image and reference projections are converted into polar coordinates followed by FT of the polar transforms generating a PFT. The correlation of the PFTs allows for very accurate determination of a capsid's orientation because it maximizes the usage of symmetry-containing information. Recently, advanced

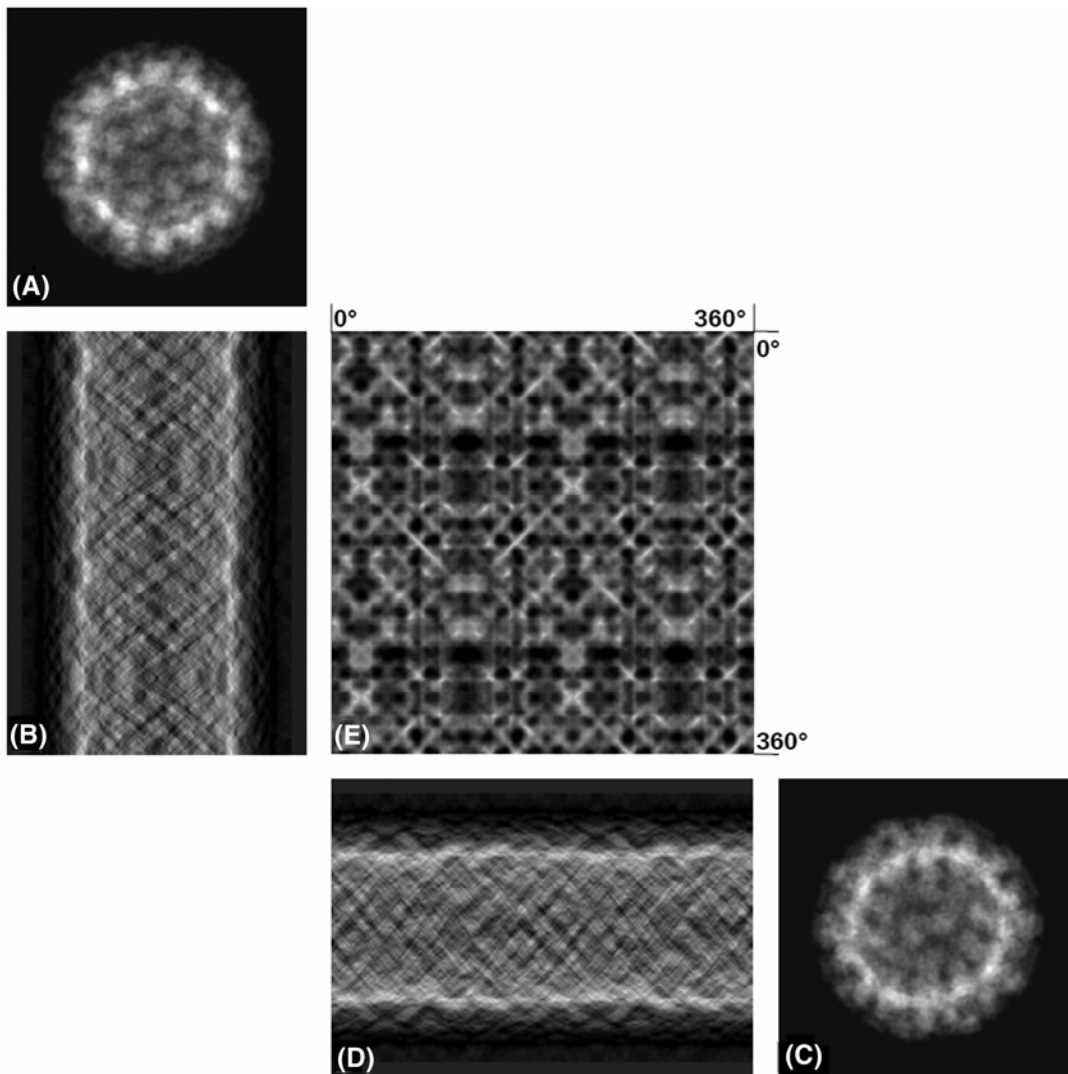


Figure 7.10. Example of real-space cross-common lines with Radon transforms. Particle #1 in (A) is compared to particle #2 in (C) by correlating their respective Radon transforms in (B) and (D), generating a correlation map (E). The correlation map reveals the orientation between the two projections through the location of its correlation peaks.

orientation determination techniques involving neural networks or Monte Carlo methods with simulated annealing have been applied. By turning random initial guesses into iterative guided searches, highly accurate orientations can be derived from random starting inputs [3,6,16].

A common technique used in orientation determination involves the usage of focal pairs. During data collection, two images of a specimen field are taken: a first image at low defocus followed by a second at high defocus. The high-defocus image contains higher contrast and better-resolved lower-spatial frequency information, which is beneficial for accurate determination

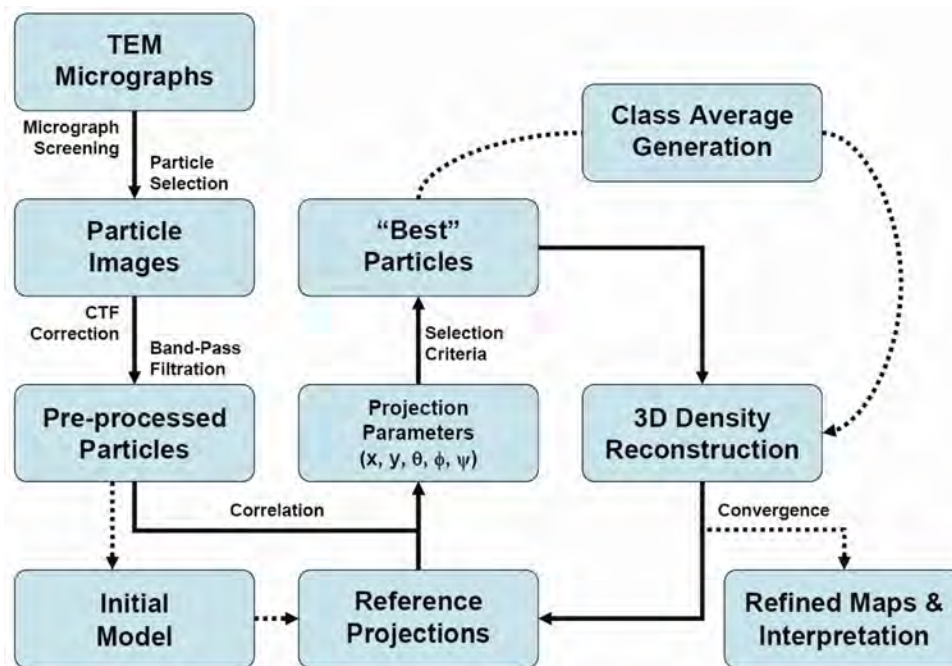


Figure 7.11. Workflow of reference-based refinement. Please visit www.springer.com/978-1-60327-232-2 to view a high-resolution full-color version of this illustration.

of orientation (Fig. 7.12). The orientation determined from the far-defocus image is then applied to the projection image from the close-to-focus image. By utilizing focal pairs in the refinement process, orientations determined from close-to-focus images whose low-spatial frequency information is limited are circumvented [2].

7.14. INITIAL MODEL GENERATION

Initial models for reference-based refinement can be generated in numerous ways. The easiest method, which mimics the molecular replacement technique in X-ray crystallography, utilizes a lowpass-filtered density map from a previously determined macromolecule. If the model chosen is close in overall shape, size, and subunit composition, it can usually serve as a successful initial model for orientation refinement. Being that the dataset should drive the overall refinement procedure, the structural details present within the dataset are expected to reveal themselves during refinement, better approximating the actual structure after each successive iteration. However, some concern for initial model bias exists. By using an inappropriate starting model, a refinement may fail to converge to its true structure as it is too strongly influenced by the model at hand and correct orientation determinations cannot be achieved. To prevent such a result, initial model bias can be circumvented by employing additional initial model generation techniques [17].

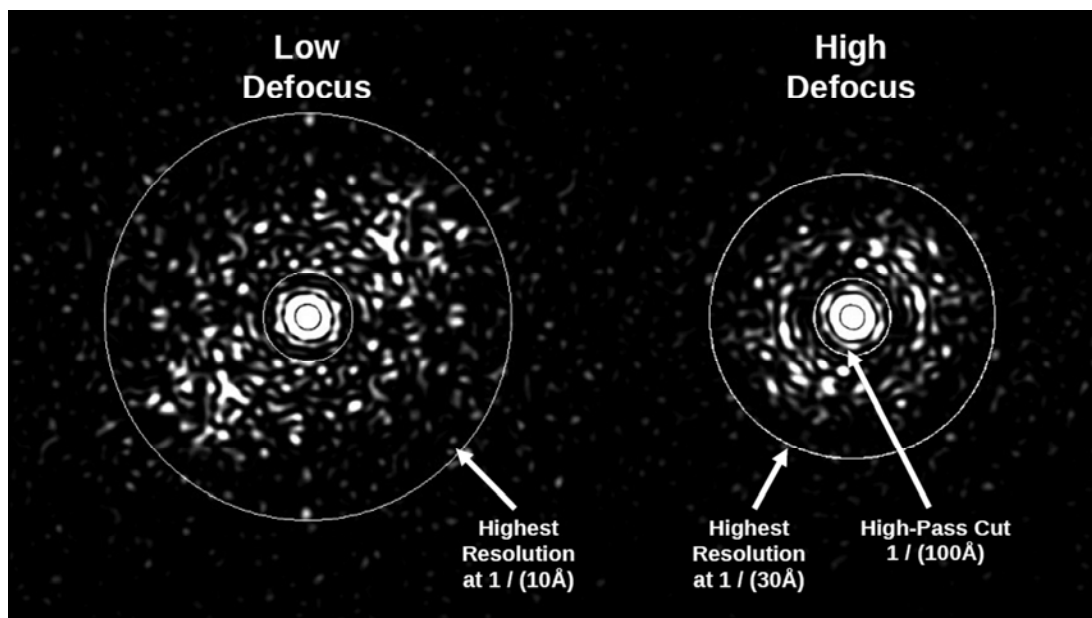


Figure 7.12. Fourier transforms derived from a focal pair of micrographs. The FT on the left was recorded at low defocus and contains high-resolution information out to $1/(10 \text{ \AA})$, while the FT on the right was recorded at high defocus and only contains high-resolution information out to $1/(30 \text{ \AA})$. The high defocus image will not be influenced by high-resolution noise during orientation refinement and should result in a more accurate orientation determination than use of the close-to-focus image.

The use of self-common lines and cross-common lines makes it possible to generate an initial model that is free of bias but contains relevant information about the structure in hand. The orientation of highly symmetric objects, such as 60-fold symmetric viral capsids, can be determined using self-common lines. Self-common lines are present within the Fourier transform of a projection image and are the result of the multiple symmetry elements present within a symmetric macromolecule (Fig. 7.13). The Fourier components along these lines will be identical to one another. An icosahedron will have 37 such pairs of self-common lines, and by applying all possible orientations to a particular image and determining the self-common lines for each, an optimal orientation can be determined for that particle. This solution can then be used to perform a single-image reconstruction to generate a starting model, or can be combined with other images of known orientation to form a noise-suppressed initial model. Unfortunately, if the particle in question does not possess a high degree of symmetry, self-common lines cannot be effectively used to determine an orientation *de novo* and cross-common lines must be used instead by determining orientations between particle images. Similar to self-common lines, the 2D FT of a projection image will share exactly one line in common with the 2D FT of another projection image. Along this line, all values of amplitude and phase will be similar between the two projections, so by searching orientation space for such a line, one can determine the relative orientation between two projection views. If multiple views are input, the overall error among all orientations is minimized in an iterative fashion. Once the orientations of these images are

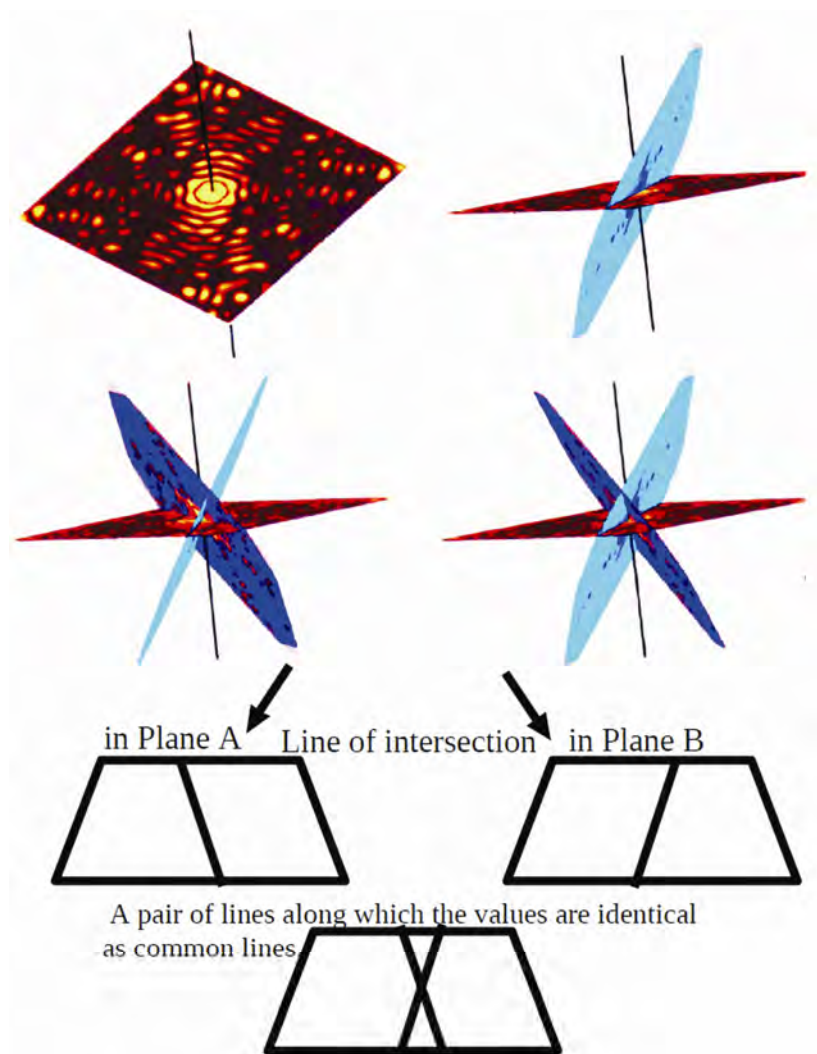


Figure 7.13. Self-common lines of a viral capsid. (A) FT of a projection oriented near the 3-fold axis. (B) Introduction of a symmetry-related projection generates a common line between the two projections. (C) Introduction of a third symmetry-related projection generates a set of three common lines, with each projection containing only two of the three possible common lines. The Fourier amplitude and phase values along these pairs of lines are identical to one another. Please visit www.springer.com/978-1-60327-232-2 to view a high-resolution full-color version of this illustration.

known, they can then be used to generate an initial model for refinement. To improve the SNR of the 2D FTs, instead of using the FT of individual images, class averages can be used. By combining the signal of numerous projection images, a more accurate cross-common line orientation can be determined [5].

A third way to generate an initial model involves the generation of a volume with a randomized Gaussian distribution. By approximating the overall shape and size of the macromolecular complex with a set of spheres or ellipsoids, a rough starting model can be generated

to seed a refinement attempt. Again, the images within the dataset should drive the refinement cycle toward the correct structure despite the fact that a very vague starting volume is used. By doing so, model bias is nearly completely eliminated, and one can be confident in their structure if consistent results are obtained from numerous random Gaussian models. This technique may fail to work if the macromolecule in question does not possess unique or significant surface features for the refinement cycle to lock on to.

Another very successful method for initial model generation is the random conical tilt. An image dataset is recorded at zero tilt within the microscope. The sample grid is then tilted and another image is recorded, albeit with the particles in different projection orientations due to the tilting. Since the angle of tilt between the two image recordings is known, the exact relationship between them can be determined, thereby defining the orientation of the images. By doing so, a relatively trustworthy and data-driven initial model is generated. A bonus with the random conical tilt is that it is able to correctly determine the handedness of the complex being studied.

7.15. RECONSTRUCTION TECHNIQUES

Once the orientations of the image projections are known, they must be combined to generate a 3D reconstruction of the object. Many techniques have been devised to accomplish this task and fall into two main categories of either transform-based or series expansion-based methods. Transform methods include weighted back projection, Fourier-Bessel inversion (common in reconstruction of icosahedral objects), and direct Fourier inversion. Transform algorithms are relatively quick to execute and are well suited to parallel processing but may suffer from Fourier-based artifacts when a solution is undersampled at a particular spatial frequency. Examples of series expansion include algebraic reconstruction techniques (ARTs) and simultaneous iterative reconstruction techniques (SIRTs). The series expansion algorithms are extremely computationally intensive, as they require the iterative solving of a large system of equations; however, they also produce the most reliable results by generating reconstruction volumes that are most consistent with the data that are input. Significant improvements have been made in the parallelization of series expansion methods, and it is likely that these techniques will become the predominant choice for volume reconstruction in SPR [18,19].

7.16. RELIABILITY ASSESSMENT

The reliability of a 3D model generated through SPR must be determined before it can be analyzed in detail. Simple checks can be performed to ensure that the reconstruction process was self-consistent. For classification-based methods, the particles within a class average should resemble the class average and their class partners. Additionally, the class average that a reference projection is matched to should reveal high similarity. For reference-based refinements, a useful trick is to perform non-reference-based classification. If non-reference-based classes match reasonably well to the classes determined through reference-based refinement, one can be confident of the consistency of the reconstructions. To eliminate the worry about initial model bias, separate reconstructions using various starting models can be performed. If a consistent solution is reached among the various starting models, it can be assured that model bias was not a factor in the reconstruction process. Also, one may track the orientation determined for a par-

ticle or set of particles throughout the refinement procedure. If a particle jumps among many orientations and never stabilizes, it is a candidate for removal from the dataset due to its unreliable behavior. Finally, it is important to determine the resolution of the final output volume. If a reconstruction is not filtered to the proper resolution, spurious details can interfere with the structural analysis and may even lead to the identification of noise-based features that are not characteristic of the actual sample. To perform a resolution check, SPR typically employs the Fourier shell correlation (FSC):

$$\text{FSC}(r) = \frac{\sum_{r \in r} F_1(r) \cdot F_2(r)^*}{\left\{ \sum_{r \in r} |F_1(r)|^2 \cdot \sum_{r \in r} |F_2(r)|^2 \right\}^{1/2}}.$$

This metric determines the summed correlation between successive shells of radial spatial frequency, r , in Fourier space of half-datasets compared against one another. The extent of their similarity in Fourier space to a correlation cutoff value of 0.5 gives a rough estimate of the resolution achieved in the reconstruction. Unfortunately, computation of the FSC from half-datasets will lead to an underestimation in achieved resolution due to halving of the dataset. Additionally, the FSC can be quite sensitive to aligned noise components or filtering artifacts, so care must be taken when assigning a reconstruction's final resolution cutoff. Debates in the field have existed over the actual numerical cutoff to use for resolution determination. Instead of the 0.5 cutoff criterion, some have suggested the use of a 3σ cutoff, where signal consistently emerges higher than random noise fluctuations, or the half-bit criterion, which is the resolution where enough information has been collected to interpret a volume. Other metrics have been developed, including Differential Phase Residual (DPR) and Spectral Signal-to-Noise Ratio (SSNR), and may be seen in publications in conjunction to an FSC curve [3,20].

7.17. ANALYSIS OF HETEROGENEITY

Several computational techniques have been developed to determine the structure of sample preparations or macromolecular complexes that are heterogeneous in nature. The first of these is termed focused classification. An initial reconstruction is performed with all of the data, followed by a 3D variance calculation. This step is able to determine which regions of the reconstructed volume exhibit the most density variance and, likely, pinpoints a region of structural flexibility within the macromolecule. By focusing in on these regions with a 3D mask and performing subsequent 2D MSA, variability in this focused region can be sorted via classification into more homogeneous datasets. These datasets are then used to generate parallel reconstructions that should characterize the structural heterogeneity present in homogeneous volumes. An offshoot of this approach is the use of 3D MSA. By generating a starting anchor set of numerous 3D reconstructions followed by 3D MSA, the structural variations present can be classified in a fashion similar to 2D MSA, generating more homogeneous subpopulations in the process. These subpopulations are then refined independently to produce a series of homogeneous reconstructions displaying the unique structural variations. A third, and perhaps the most complicated and computationally intensive approach, involves the use of Maximum Likelihood in the refinement process. A starting anchor set of numerous random models are generated, followed by independent maximum-likelihood refinement of the random models. Through its iterative pro-

cedure, the maximum-likelihood algorithm will progressively choose particles that most accurately match one of the 3D references they are being compared to. If structural variations are indeed present, homogeneous datasets will “self-crystallize” themselves computationally from the starting dataset by grouping with one of the various models throughout consecutive iterations [21–23].

7.18. SUMMARY

Transmission electron microscopy has seen a recent boom in its usage for macromolecular structural determination. Advances in electron microscope design, sample preparation techniques, and in refinement and reconstruction algorithms have pushed the resolution capabilities of SPR to nearly the 3-Å range. At this resolution, alpha-helices and beta-strands can be easily resolved. Additionally, de novo peptide backbone traces can be performed with high accuracy, and even bulky aromatic sidechains can be identified. Further efforts in SPR will concentrate on massively parallel refinements involving the usage of tens of thousands to hundreds of thousands of particles to push the resolution limit even further and to truly challenge the resolution achieved by XRD or NMR.

ACKNOWLEDGMENTS

Thanks to Dr. M. Kawano for help with the figure sets.

PROBLEMS

- 7.1. What fraction of the speed of light is the velocity of an electron experiencing an accelerating voltage of 200 kV? What is the relativistic mass of an electron accelerated to 1000 kV? Why are these values significant? [Adapted from Williams D, Carter C. 1996. *Transmission electron microscopy: Basics I*. New York: Springer.]
- 7.2. Given that $\gamma(s) = -\sin\left[\frac{\pi}{2}C_s\lambda^3s^4 + \pi\Delta z\lambda s^2\right]$, how would the introduction of a Zernike-like phase plate at the back focal plane affect the CTF if the phase plate imparts a $-\pi/2$ phase shift? Why would this be beneficial? [Adapted from Danev R, Nagayama K. 2001. Transmission electron microscopy with Zernike phase plate. *Ultramicroscopy* **88**:243–252.]
- 7.3. In cylindrical coordinates, a particle's density and its transform are related by $p(r, \phi, z) = \sum_n \int g_n \exp^{in\phi} \exp^{2\pi i z Z} dZ$. The Fourier-Bessel transform of g_n is given by $G_n(R, Z) = \int_0^\infty g_n(r, Z) J_n(2\pi Rr) 2\pi R dr$. The representation for transform data with discrete sampling is $F_j = \sum_{n=-N}^N B_{jn} G_n$ ($n = -N \dots N$), with F_j being the available values of the transform independent of the particle density, B_{jn} the sampling matrix of the transform, and G_n the

Fourier transform of the particle density, and the solution being $G_n = \frac{1}{2m} \sum_{j=1}^{2m} B_{km}^* F_j$ ($n = -N \dots N$). Assuming that (1) the data provided are evenly spaced and (2) there are as many observations F_j as unknowns G_n ($2m \geq 2N + 1$), what is the minimum number of views, m , required to reconstruct a particle of diameter D to a given resolution d ($= 1/R_{\max}$)? [Adapted from Crowther R, DeRosier D, Klug A. 1970. The reconstruction of a three-dimensional structure from projections and its application to electron microscopy. *Proc R Soc A* **317**(1530):319–240.]

FURTHER READING

- Baker T, Olson N, Fuller S. 1999. Adding the third dimension to virus life cycles: three-dimensional reconstruction of icosahedral viruses from cryo-electron micrographs. *Microbiol Mol Biol Rev* **63**(4):862–922.
- Cheng RH, Hammar L. 2004. *Conformational proteomics of macromolecular architectures*, Singapore: World Scientific. ISBN 981-238-614-9
- Frank J. 2006. *Three-dimensional electron microscopy of macromolecules*. New York: Oxford UP.
- Orlov I, Morgan DG, Cheng RH 2006. Efficient implementation of a filtered back-projection algorithm using a voxel-by-voxel approach. *J Struct Biol* **154**:287–296
- Scherzer O. 1949. The theoretical resolution limit of the electron microscopy. *J Appl Phys* **20**(1):20–29.
- Williams D, Carter C. 1996. *Transmission electron microscopy: basics I*. New York: Springer.

REFERENCES

1. Baker TS, Olson NH, Fuller SD. 1999. Adding the third dimension to virus life cycles: three-dimensional reconstruction of icosahedral viruses from cryo-electron micrographs. *Microbiol Mol Biol Rev* **63**(4):862–922.
2. Cheng RH, Olson NH, Baker TS. 1992. Cauliflower mosaic virus: a 420 subunit ($T = 7$), multilayer structure. *Virology* **186**(2):655–668.
3. Cheng RH, Reddy VS, Olson NH, Fisher AJ, Baker TS, Johnson JE. 1994. Functional implications of quasi-equivalence in a $T = 3$ icosahedral animal virus established by cryo-electron microscopy and X-ray crystallography. *Structure* **2**(4):271–282.
4. Crowther RA, Amos LA, Finch JT, De Rosier DJ, Klug A. 1970. Three-dimensional reconstructions of spherical viruses by Fourier synthesis from electron micrographs. *Nature* **226**(5244):421–425.
5. Fuller SD, Butcher SJ, Cheng RH, Baker TS. 1996. Three-dimensional reconstruction of icosahedral particles—the uncommon line. *J Struct Biol* **116**(1):48–55.
6. Baker TS, Cheng RH. 1996. A model-based approach for determining orientations of biological macromolecules imaged by cryoelectron microscopy. *J Struct Biol* **116**(1):120–130.
7. Gong ZX, Wu H, Cheng RH, Hull R, Rossmann MG. 1990. Crystallization of cauliflower mosaic virus. *Virology* **179**(2):941–945.
8. Fujiyoshi Y. 1989. High resolution cryo-electron microscopy for biological macromolecules. *J Electron Microscop (Tokyo)* **38**(Suppl):S97–S101.
9. Booth CR, Jakana J, Chiu W. 2006. Assessing the capabilities of a 4k x 4k CCD camera for electron cryo-microscopy at 300 kV. *J Struct Biol* **156**(3):556–563.
10. Chen DH, Jakana J, Liu X, Schmid MF, Chiu W. 2008. Achievable resolution from images of biological specimens acquired from a 4k x 4k CCD camera in a 300-kV electron cryomicroscope. *J Struct Biol* **163**(1):45–52.
11. Ludtke SJ, Baldwin PR, Chiu W. 1999. EMAN: semiautomated software for high-resolution single-particle reconstructions. *J Struct Biol* **128**(1):82–97.
12. Sines J, Rothnagel R, van Heel M, Gaubatz JW, Morrisett JD, Chiu W. 1994. Electron cryomicroscopy and digital image processing of lipoprotein(a). *Chem Phys Lipids* **67–68**:81–89.
13. Schatz M, van Heel M. 1990. Invariant classification of molecular views in electron micrographs. *Ultramicroscopy* **32**(3):255–264.

14. van Heel M, Harauz G, Orlova EV, Schmidt R, Schatz M. 1996. A new generation of the IMAGIC image processing system. *J Struct Biol* **116**(1):17–24.
15. Serysheva, II, Orlova EV, Chiu W, Sherman MB, Hamilton SL, van Heel M. 1995. Electron cryomicroscopy and angular reconstitution used to visualize the skeletal muscle calcium release channel. *Nat Struct Biol* **2**(1):18–24.
16. Cheng RH, Kuhn RJ, Olson NH, Rossmann MG, Choi HK, Smith TJ, Baker TS. 1995. Nucleocapsid and glycoprotein organization in an enveloped virus. *Cell* **80**(4):621–630.
17. Wikoff WR, Wang G, Parrish CR, Cheng RH, Strassheim ML, Baker TS, Rossmann NG. 1994. The structure of a neutralized virus: canine parvovirus complexed with neutralizing antibody fragment. *Structure* **2**(7):595–607.
18. Crowther RA, Klug A. 1971. ART and science or conditions for three-dimensional reconstruction from electron microscope images. *J Theor Biol* **32**(1):199–203.
19. Orlov IM, Morgan DG, Cheng RH. 2006. Efficient implementation of a filtered back-projection algorithm using a voxel-by-voxel approach. *J Struct Biol* **154**(3):287–296.
20. van Heel M, Schatz M. 2005. Fourier shell correlation threshold criteria. *J Struct Biol* **151**(3):250–262.
21. Zhou ZH, Liao W, Cheng RH, Lawson JE, McCarthy DB, Reed LJ, Stoops JK. 2001. Direct evidence for the size and conformational variability of the pyruvate dehydrogenase complex revealed by three-dimensional electron microscopy: the "breathing" core and its functional relationship to protein dynamics. *J Biol Chem* **276**(24):21704–21713.
22. Haag L, Garoff H, Xing L, Hammar L, Kan ST, Cheng RH. 2002. Acid-induced movements in the glycoprotein shell of an alphavirus turn the spikes into membrane fusion mode. *EMBO J* **21**(17):4402–4410.
23. Xing L, Casasnovas JM, Cheng RH. 2003. Structural analysis of human rhinovirus complexed with ICAM-1 reveals the dynamics of receptor-mediated virus uncoating. *J Virol* **77**(11):6101–6107.

